RSC Advances

PAPER

View Article Online
View Journal | View Issue

Cite this: *RSC Adv.*, 2026, **16**, 29712

Effect of the Nd promoter on precipitated iron-based catalysts for high-temperature Fischer–Tropsch synthesis of light olefins

Yi Yang, [ab] Fengping Yu,[b] Delong Ding,[b] Chunliang Ge, *[b] Biao Chen,[b] Xiaojiong Wu,[b] Yaoji Chen,[b] Hanfeng Lu, [a] Hongfang Ma, [c] Haitao Zhang, [c] Weixin Qian [c] and Weiyong Ying [c]

To explore the influence of the rare earth element neodymium (Nd) on the production of light olefins ($C_2^=$–$C_4^=$) *via* high-temperature Fischer–Tropsch synthesis (HTFT), a series of FeMn-based catalysts promoted with Nd and Na were synthesized using a combination of coprecipitation and incipient wetness impregnation techniques. These included Nd-modified FeMnxNd (x = 0, 0.1, 0.4, 0.7, 1, and 2), FeMnNa, and FeMn0.7NdNa catalysts. The results indicate that Nd reduces catalyst particle size and increases the BET specific surface area. Nd enhances surface basicity, increases the electron density around Fe atoms, suppresses hydrogen adsorption, and promotes CO dissociative adsorption, thereby facilitating the formation of χ-Fe_5C_2 and improving Fischer–Tropsch synthesis (FTS) activity. However, excessive Nd loading results in Nd deposition on the catalyst surface, which decreases the BET surface area, induces particle agglomeration and growth, and inhibits catalyst reduction and carburization. These effects collectively reduce the content of χ-Fe_5C_2 and lead to inferior FTS performance. In contrast, the synergistic interaction of Nd–Na suppresses the formation of θ-Fe_3C, prevents particle agglomeration, and enhances the content of χ-Fe_5C_2, thereby significantly increasing CO conversion and light olefin yield. The FeMn0.7NdNa catalyst achieves a light olefin yield of 412.1 g h^{-1} kg_{Cat}^{-1}, markedly surpassing that of FeMn0.7Nd and FeMnNa.

Received 8th April 2026
Accepted 25th May 2026

DOI: 10.1039/d6ra02950g

rsc.li/rsc-advances

1. Introduction

Light olefins ($C_2^=$–$C_4^=$) are fundamental building blocks in the chemical industry, serving as key intermediates in the production of a wide array of commodities—ranging from polymers and surfactants to pharmaceuticals and cosmetic ingredients.[1,2] Traditionally, these olefins are produced *via* petroleum-derived routes; however, growing environmental and economic concerns have spurred significant interest in alternative non-petroleum pathways.[3–5] Fischer–Tropsch synthesis (FTS) is a catalytic process that converts syngas into a wide range of hydrocarbons and oxygenates.[6] Its ability to utilize syngas derived from coal, natural gas, or biomass makes it a particularly attractive sustainable route for the direct production of olefins.[7,8] Compared to low-temperature Fischer–Tropsch (LTFT), the high-temperature process (HTFT) shifts product selectivity toward lighter hydrocarbons, thereby enhancing $C_2^=$–$C_4^=$ olefin formation while preserving favorable energy and cost efficiency.[9,10]

It is well established that the introduction of alkali, transition, or rare earth metals as promoters can influence the catalytic behavior of FTS catalysts, enabling enhanced light olefin selectivity, increased activity, and improved stability.[9,11–18] Research on rare earth metals as promoters in FTS catalysts remains relatively scarce. Han *et al.*[11] demonstrated that rare earth promoters (La, Ce, Nd, Sm, Eu) enhance the performance of iron-based FTS catalysts through electron donation to Fe species. This electronic modification strengthens CO dissociative adsorption and promotes χ-Fe_5C_2 formation, thereby improving light olefin selectivity. Among the elements tested, Nd proved most effective in boosting both activity and olefin selectivity, with Sm ranking second. Zeng *et al.*[19] further examined the role of Nd in FTS catalysts and reported that Nd addition significantly increases the selectivity to light hydrocarbons while reducing C_5^+ selectivity. Similarly, Nie *et al.*[20] synthesized FeCe catalysts for FTS. Their results demonstrate that an optimal amount of Ce exerts multiple beneficial effects: it improves the dispersion of iron species, increases the specific surface area, and acts as an electron donor, thereby raising the electron density around surface Fe atoms. These effects collectively strengthen CO dissociative adsorption,

[a]*Innovation Team of Air Pollution Control, Institute of Catalytic Reaction Engineering, State Key Laboratory Breeding Base of Green Chemistry Synthesis Technology, College of Chemical Engineering, Zhejiang University of Technology, Hangzhou 310014, China*

[b]*Zhejiang Zheneng Technology & Environment Group Co., Ltd, Hangzhou, 311100, China. E-mail: gechunliang@zhenergy.com.cn*

[c]*Engineering Research Center of Large Scale Reactor Engineering and Technology, Ministry of Education, State Key Laboratory of Chemical Engineering, School of Chemical Engineering, East China University of Science and Technology, Shanghai 200237, China*

elevate the content of χ-Fe_5C_2, and consequently enhance both FTS activity and $C_2^=$–$C_4^=$ selectivity. Burgun *et al.*[12] synthesized FeCu-based FTS catalysts supported on mordenite and modified with rare earth metals, including Ce, Nd, Ho, Er. The results demonstrated that Nd steered selectivity toward light olefins, whereas Ho mitigated the formation of longer-chain hydrocarbons and carbonaceous deposits. Wang *et al.*[13] demonstrated that sodium and manganese exert contrasting yet complementary effects in iron-based FTS catalysts. Sodium increases Fe_2O_3 particle size and suppresses reduction *via* enhanced basicity, whereas manganese reduces particle size. The synergistic effect of Na and Mn improves the selectivity for long-chain hydrocarbons and light olefins.

The roles of rare earth metal Nd and its synergistic interaction with Na in the HTFT of light olefins remain largely unexplored. In this work, FeMn catalysts modified with Nd and Na were synthesized *via* a two-step synthesis route involving coprecipitation and impregnation. The catalytic performance was evaluated in a fixed-bed reactor under HTFT conditions, with particular focus on the influence of Nd content and Nd–Na synergy on activity, and $C_2^=$–$C_4^=$ selectivity.

2. Experiments

2.1. Catalysts preparation

The FeMn*x*Nd catalysts were synthesized *via* the coprecipitation method. An aqueous solution containing $Fe(NO_3)_3\cdot 9H_2O$ (99.99 wt% purity, Aladdin), $Mn(NO_3)_2$ (50 wt% purity, Aladdin), and $Nd(NO_3)_3\cdot 6H_2O$ (99.99 wt% purity, Aladdin) in the desired molar ratios served as the metal source, while an ammonia solution (25–28%, AR, Aladdin) was used as the precipitating agent. The mixed metal nitrate solution and the ammonia solution were simultaneously added dropwise into a beaker under continuous stirring at 65 °C. Following precipitation, the slurry was kept under stirring for another 1 h, after which the slurry was left to age for 4 h. The precipitate was then washed with deionized water until the filtrate reached neutrality, dried at 110 °C for 12 h, and finally calcined at 500 °C for 4 h. The coprecipitated FeMn*x*Nd catalysts have a molar composition of 100Fe/5Mn/*x*Nd ($x = 0$, 0.1, 0.4, 0.7, 1, and 2) and are labeled as FeMn, FeMn0.1Nd, FeMn0.4Nd, FeMn0.7Nd, FeMn1Nd, and FeMn2Nd, respectively.

The FeMnNa catalyst has a molar composition of 100Fe/5Mn/2Na and is labeled as FeMnNa. The FeMn0.7NdNa catalyst has a molar composition of 100Fe/5Mn/0.7Nd/2Na and is labeled as FeMn0.7NdNa. The FeMnNa and FeMn0.7NdNa catalysts were prepared *via* impregnation. Specifically, the FeMn and FeMn0.7Nd precursors were impregnated with an aqueous solution of $NaNO_3$ (99.99% purity, Aladdin) at the desired concentration. After impregnation, the catalysts were aged at room temperature for 24 h, subsequently dried at 110 °C for 12 h, and calcined at 500 °C for 4 h in air.

2.2. Catalysts characterization

X-ray diffraction (XRD) patterns were recorded on a D/MAX2550 VB/PC diffractometer over a 2θ range from 10° to 80°.

Argon physisorption measurements were performed at −186 °C using an ASAP 2020 instrument. Each sample (≈200 mg) was degassed under vacuum at 350 °C for 5 h. Surface area measurements were determined from the adsorption branch using the Brunauer–Emmett–Teller (BET) model.

Transmission electron microscopy (TEM) images were obtained using a JEM-2100F microscope operating at an acceleration voltage of 200 kV. Elemental mapping was carried out using an FEI Talos F200X microscope equipped with an energy-dispersive X-ray spectroscopy (EDS) detector.

X-ray photoelectron spectroscopy (XPS) measurements were performed using an ESCALAB 250XI spectrometer equipped with a monochromatic Al Kα X-ray source operating at a power of 150 W.

Temperature-programmed reduction (H_2-TPR) experiments were carried out on an AutoChem II 2920 instrument. Prior to each measurement, approximately 50 mg of sample was purged under an argon flow at 350 °C for 1 h, then cooled to 60 °C. Subsequently, the sample was heated to 800 °C at a ramping rate of 10 °C min^{-1} under a continuous flow of 10% H_2/Ar (v/v) mixture.

The temperature-programmed desorption experiments—including CO-TPD, H_2-TPD, and CO_2-TPD—were also performed using the AutoChem II 2920 system. Approximately 200 mg of sample was first reduced in a H_2 atmosphere at 350 °C for 5 h. After cooling to 60 °C, the sample was saturated with the corresponding probe gas—either 5% CO/He, 10% H_2/Ar, or 5% CO_2/He (v/v)—for 30 min. Subsequently, the system was purged with pure He for an additional 30 min. Desorption was then carried out by heating the sample to 800 °C at a rate of 10 °C min^{-1} under a continuous He flow, while the desorption profile was recorded.

The iron species present in the spent catalysts were characterized by Mössbauer spectroscopy, using a constant-acceleration MR-351 spectrometer equipped with a ^{57}Co(Pd) source.

2.3. Catalysts evaluation

A fixed bed stainless steel reactor is used to evaluate FTS. 0.3 g of catalyst was loaded into the isothermal zone of the reactor. The catalyst underwent reduction under a H_2 stream at a flow rate of 6000 mL h^{-1} g_{Cat}^{-1}, at 350 °C and atmospheric pressure (0.1 MPa) for 10 h. Following reduction, the FTS was conducted at 320 °C and 1.0 MPa, using a syngas feed with a H_2/CO molar ratio of 2 and a gas hourly space velocity of 12 000 mL h^{-1} g_{Cat}^{-1}. While the gaseous effluents were analyzed real-time through *in situ* GC analysis (Agilent 7890A), the liquids and waxy products were collected and analyzed separately by the same instrument. The corresponding calculation was performed according to eqn (1)–(3).

$$X_{CO}(\%) = \frac{N_{in,CO} - N_{out,CO}}{N_{in,CO}} \times 100\% \quad (1)$$

$$S_{CO_2}(\%) = \frac{N_{out,CO_2}}{N_{in,CO} - N_{out,CO}} \times 100\% \quad (2)$$

$$S_{C_iH_j}(\%) = \frac{iN_{out,C_iH_j}}{\sum_{i=1}^{n} iN_{out,C_iH_j}} \times 100\% \quad (3)$$

3. Results and discussion

3.1. Structure and morphology

Table 1 summarizes the textural properties of all fresh catalysts. As the Nd content increases from 0 to 0.7%, the BET specific surface area of the FeMn*x*Nd catalysts progressively rises from 24.4 $m^2\ g^{-1}$ to 33.1 $m^2\ g^{-1}$, accompanied by a decrease in average pore size from 20.7 nm to 16.6 nm. Upon further increasing the Nd content from 0.7% to 2%, the BET specific surface area of the FeMn*x*Nd catalysts exhibits a decline from 33.1 $m^2\ g^{-1}$ to 25.9 $m^2\ g^{-1}$, while the average pore size correspondingly expands from 16.6 nm to 22.6 nm. It indicates that the introduction of moderate amount of Nd promoter plays the role of structural additive, which makes the catalyst have higher BET specific surface area and enhanced active phase dispersion, while the introduction of excessive Nd additive, the excess Nd is enriched on the catalyst surface, leading to a reduced BET specific surface area.[21] The FeMn0.7Nd catalyst has the largest BET specific surface area and the smallest average pore size. Smaller pore sizes in mesoporous catalysts improve the dispersion of iron oxides, whereas larger pore sizes encourage agglomeration of iron oxides, leading to larger iron particles.[22] Comparison of FeMnNa catalysts and FeMn0.7Nd, FeMn0.7NdNa catalysts illustrates that adding Na to the catalyst leads to a decline in BET specific surface area.

Fig. 1 presents the XRD patterns of the fresh catalysts. All samples exhibit characteristic diffraction peaks corresponding to the α-Fe_2O_3 phase. A gradual reduction in average crystallite size is observed as the Nd content is elevated from 0 to 0.7%, with values dropping from 30.6 nm to 21.6 nm. However, further increasing the Nd content from 0.7% to 2% leads to an increase in crystallite size from 21.6 nm to 29.3 nm. It indicates that the introduction of moderate amount of Nd reduces the average grain size of catalyst, which is favorable to improving the dispersion of Fe_2O_3 nanoparticles, while the introduction of excessive Nd results in the enrichment of excessive Nd on the catalyst surface, leading to an increase in the catalyst average grain size.

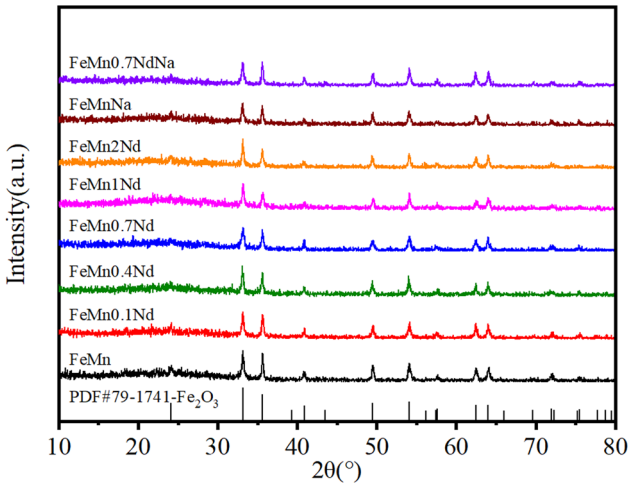

Fig. 1 XRD patterns of fresh catalysts.

The morphology and nanostructure of the catalysts were investigated by TEM (Fig. 2). All samples feature near-spherical nanoparticles with sizes between 10 and 50 nm. However, for the FeMn catalyst prepared without Nd modification, noticeable agglomeration occurs alongside a tendency toward larger particle sizes. In contrast, the Fe_2O_3 particles are better dispersed in the FeMn0.7Nd catalyst, and the catalyst particle size is smaller. Upon raising the Nd content to 2%, the FeMn2Nd catalyst reverts to a state of pronounced particle agglomeration, alongside a coarsening of particle size. This observation can be attributed to the surface enrichment of excess Nd species, which tends to promote agglomeration of Fe_2O_3 particles—a finding consistent with the trends observed in both BET surface area and XRD crystallite size measurements. It indicates that the introduction of moderate amount of Nd reduces the catalyst particle size and is beneficial to improve the dispersion of Fe_2O_3 nanoparticles, while the excessive Nd loading results in particle agglomeration and enlarged catalyst particle sizes.

Table 1 Textural property of catalysts

Catalyst	S_{BET}[a] ($m^2\ g^{-1}$)	V_P[b] ($cm^3\ g^{-1}$)	D_P[c] (nm)	$d_{Fe_2O_3}$[d] (nm)
FeMn	24.4	0.18	20.7	30.6
FeMn0.1Nd	24.9	0.19	21.4	30.2
FeMn0.4Nd	28.5	0.20	17.0	29.6
FeMn0.7Nd	33.1	0.20	16.6	21.6
FeMn1Nd	31.7	0.20	17.2	29.4
FeMn2Nd	25.9	0.22	22.6	29.3
FeMnNa	18.8	0.19	27.9	24.9
FeMn0.7NdNa	20.7	0.19	25.1	26.2

[a] BET specific surface area. [b] BJH desorption pore volume. [c] BJH desorption average pore size. [d] Crystallite size estimated using the Scherrer equation from the (104) diffraction peak of Fe_2O_3 ($2\theta \approx 33.16°$).

3.2. Electronic effect

The surface composition and chemical states of the catalysts were investigated by XPS, with the corresponding spectra shown in Fig. 3. The Fe 2p region is characterized by two main peaks located at 723.9 eV and 710.7 eV, assigned to the Fe $2p_{1/2}$ and Fe $2p_{3/2}$ levels, respectively.[23,24] Fig. 3a illustrates the evolution of Fe 2p binding energies as a function of Nd loading. When the Nd content rises from 0 to 2%, the Fe $2p_{1/2}$ peak shifts from 723.9 eV to 723.6 eV, and the Fe $2p_{3/2}$ peak shifts from 710.7 eV to 710.4 eV. This downward shift in binding energy is consistent with literature reports indicating an enhanced electron density around the Fe species.[25] This observation can be attributed to the lower electronegativity of Nd compared to Fe. Thus, electron

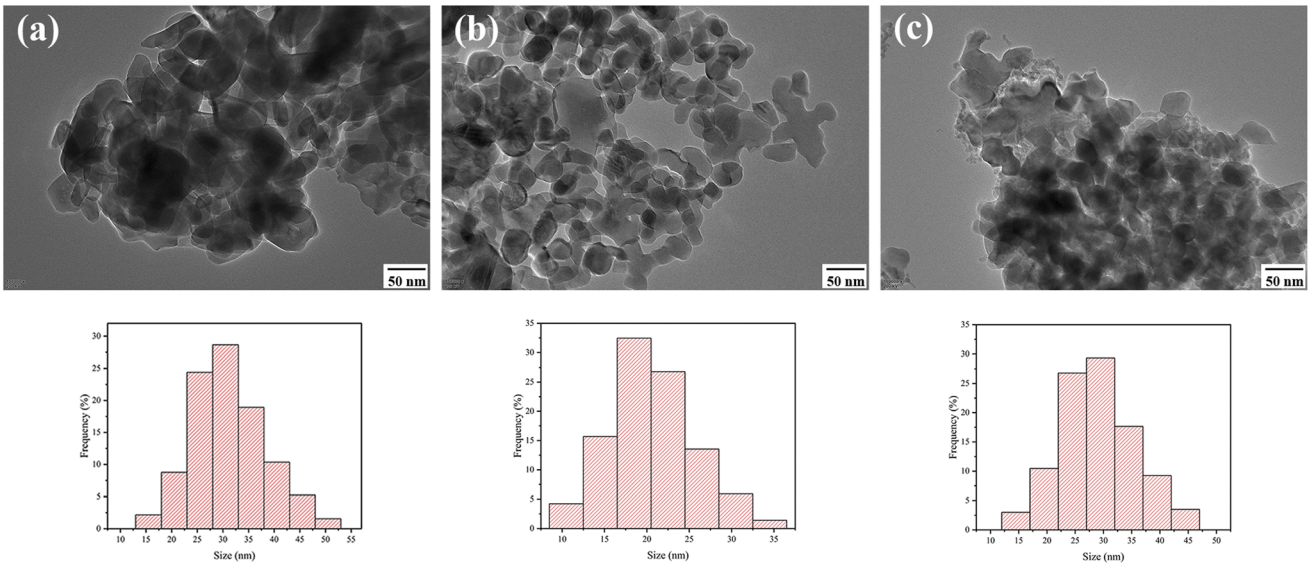

Fig. 2 TEM images (a) FeMn, (b) FeMn0.7Nd, (c) FeMn2Nd.

donation from Nd to Fe enhances the electron density on Fe atoms, which in turn lowers the Fe 2p binding energy.[11]

In Fig. 3b, the addition of Na leads to a slight decrease in the Fe 2p binding energies. In comparison with the unmodified FeMn, the FeMnNa sample exhibits Fe $2p_{1/2}$ and Fe $2p_{3/2}$ binding energies of 723.8 eV and 710.6 eV, shifted downward from 723.9 eV and 710.7 eV. Similarly, when Na is introduced into the FeMn0.7Nd catalyst, the resulting FeMn0.7NdNa sample shows further reductions in binding energy, with Fe $2p_{1/2}$ decreasing from 723.7 eV to 723.5 eV and Fe $2p_{3/2}$ from 710.6 eV to 710.3 eV. The XPS results reveal that Na addition markedly promotes electron enrichment on Fe atoms. Significantly, the co-promoted FeMn0.7NdNa catalyst shows the lowest Fe 2p binding energies among all samples, indicating the highest Fe surface electron density. The observed enhancement reflects the Nd–Na synergy, one that goes beyond the simple sum of their individual promotional effects.

3.3. Reducibility of the catalysts

The reduction behavior of the fresh catalysts was investigated by H_2-TPR, with the corresponding profiles shown in Fig. 4. As shown in Fig. 4a and b, two distinct reduction stages are observed for all samples. The low-temperature peak appearing in the range of 250–350 °C corresponds to the reduction of α-Fe_2O_3 to Fe_3O_4,[26] while the high-temperature feature between 350 and 700 °C is associated with the subsequent reduction of Fe_3O_4 to FeO and ultimately to metallic α-Fe.[27] Examining the effect of Nd promotion (Fig. 4a), a progressive shift of both reduction peaks toward higher temperatures is evident as the Nd content increases from 0 to 2%. This upward shift suggests that Nd incorporation strengthens the Fe–O bond, thereby inhibiting the reducibility of α-Fe_2O_3. Moreover, the extent of this inhibition becomes more pronounced with higher Nd loadings. The observed Fe–Nd interactions appear to render the samples more resistant to reduction, which may contribute positively to the structural stability of the catalysts during reaction. Complementing the XPS findings discussed earlier, the increased reduction temperatures for Nd-promoted samples may also be rationalized in terms of electronic effects. The increased electron density on surface Fe atoms induced by Nd addition may weaken hydrogen adsorption, consequently slowing reduction kinetics and shifting reduction peaks to higher temperatures.[28]

Fig. 4b reveals that relative to FeMn and FeMn0.7Nd, the reduction peaks of FeMnNa and FeMn0.7NdNa appear at elevated temperatures upon Na addition. This upward shift indicates that the presence of Na suppresses the reducibility of α-Fe_2O_3, consistent with a stabilizing effect on the iron oxide phase. Notably, among all samples, the FeMn0.7NdNa catalyst—promoted with both Nd and Na—exhibits the highest reduction peak temperatures, surpassing those of FeMnNa and FeMn0.7Nd. This observation points to the synergistic interaction between Nd and Na, whereby their combined presence further suppresses the reducibility of α-Fe_2O_3 beyond the level achieved by either promoter alone.

3.4. Chemisorption properties

3.4.1. CO chemisorption. The CO adsorption properties of the reduced catalysts were investigated by CO-TPD, with the resulting profiles shown in Fig. 5. According to previous studies, desorption peaks centered around 100 °C are typically associated with molecularly adsorbed CO, whereas peaks appearing above 350 °C arise from dissociative CO adsorption.[29–31] As shown in Fig. 5a, while all eight catalysts exhibit similar molecular CO desorption features, marked differences are observed in the high-temperature region corresponding to CO dissociative adsorption. For the FeMn*x*Nd series, increasing the Nd content from 0 to 0.7% leads to a progressive enlargement of the dissociative CO desorption peak area, accompanied by a shift toward higher temperatures. This trend indicates that

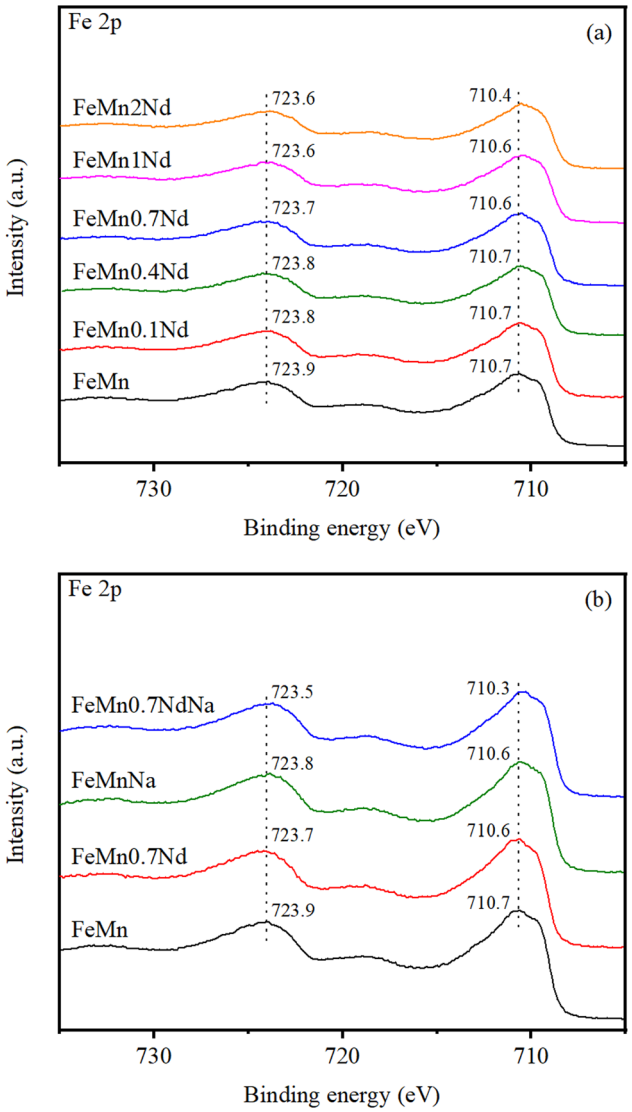

Fig. 3 XPS spectra of the catalysts.

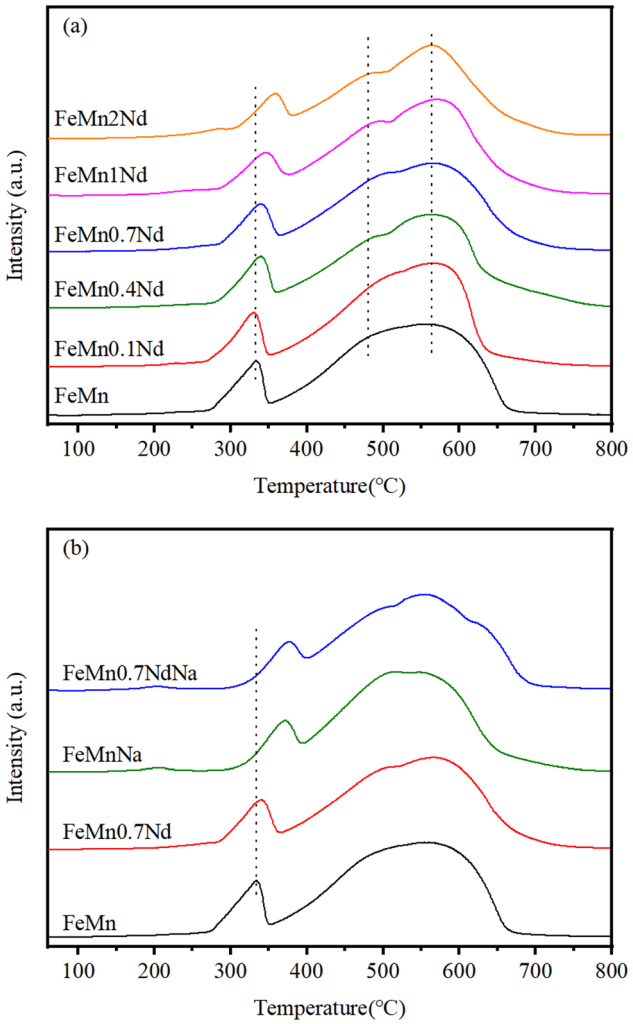

Fig. 4 H_2-TPR profiles of the samples.

moderate Nd promotion enhances the dissociative adsorption of CO. In line with the XPS results, the increased electron cloud density on Fe atoms in Nd-modified catalysts appears to facilitate CO dissociation.[11,32] However, upon further increasing the Nd content from 0.7% to 2%, a noticeable decline in the CO dissociative desorption peak area is observed. Correlating with the BET, XRD, and TEM findings, this decline can be attributed to the surface enrichment of excess Nd species, which induces particle agglomeration and increased crystallite size. These morphological changes likely result in the coverage or blocking of active sites, thereby reducing the catalyst's capacity for CO dissociative adsorption.

As depicted in Fig. 5b, the CO dissociative adsorption capacity is substantially enhanced upon Na addition for both FeMnNa and FeMn0.7NdNa when compared to FeMn and FeMn0.7Nd. This enhancement is evidenced by the progressive increase in the area of the high-temperature CO desorption peak and its concomitant shift toward higher temperatures, indicating that Na promotion facilitates CO dissociation. Remarkably, the FeMn0.7NdNa containing both Nd and Na promoters exhibits the strongest CO dissociative desorption capability. This finding provides strong evidence for a synergistic interaction between Nd and Na, wherein their combined presence promotes CO dissociative adsorption beyond the level achievable by either promoter alone.

3.4.2. H_2 chemisorption. In Fig. 6, the hydrogen adsorption behavior of the reduced catalysts was investigated by H_2-TPD. All samples exhibit three distinct desorption features. The low-temperature peak centered at approximately 100 °C, denoted as H_α, corresponds to hydrogen species weakly adsorbed in shallow surface sites. The intermediate peak around 150 °C, labeled H_β, is attributed to hydrogen adsorbed on deeper sites or defects associated with metallic Fe. Hydroxyl species adsorbed on unreduced oxide phases decompose above 250 °C, producing the desorption feature referred to as $H\gamma$.[30,33,34] Upon Nd incorporation, a marked reduction in the integrated areas of both H_α and H_β peaks is observed relative to the unmodified FeMn catalyst. This indicates that Nd suppresses the adsorption of hydrogen species. Consistent with the XPS findings,

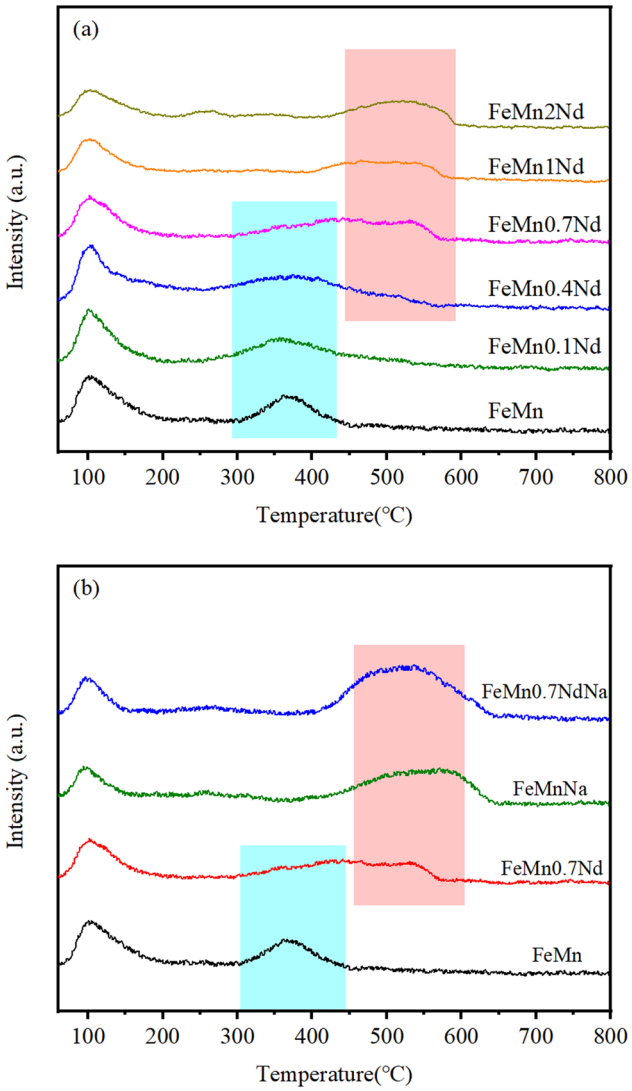

Fig. 5 CO-TPD curves of the reduced catalysts.

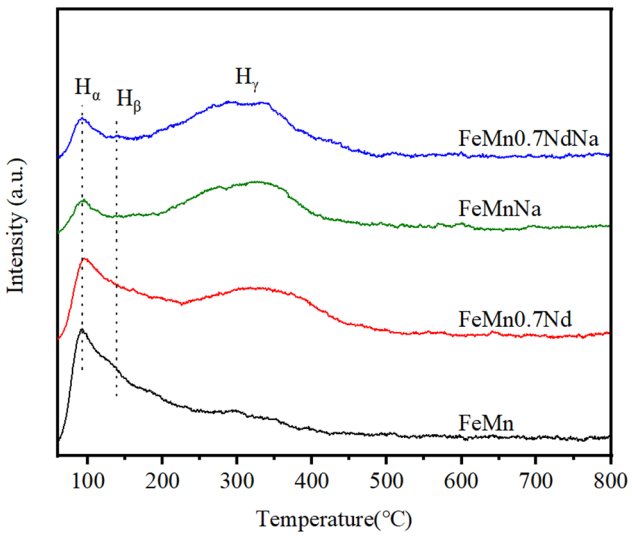

Fig. 6 H_2-TPD curves of the reduced catalysts.

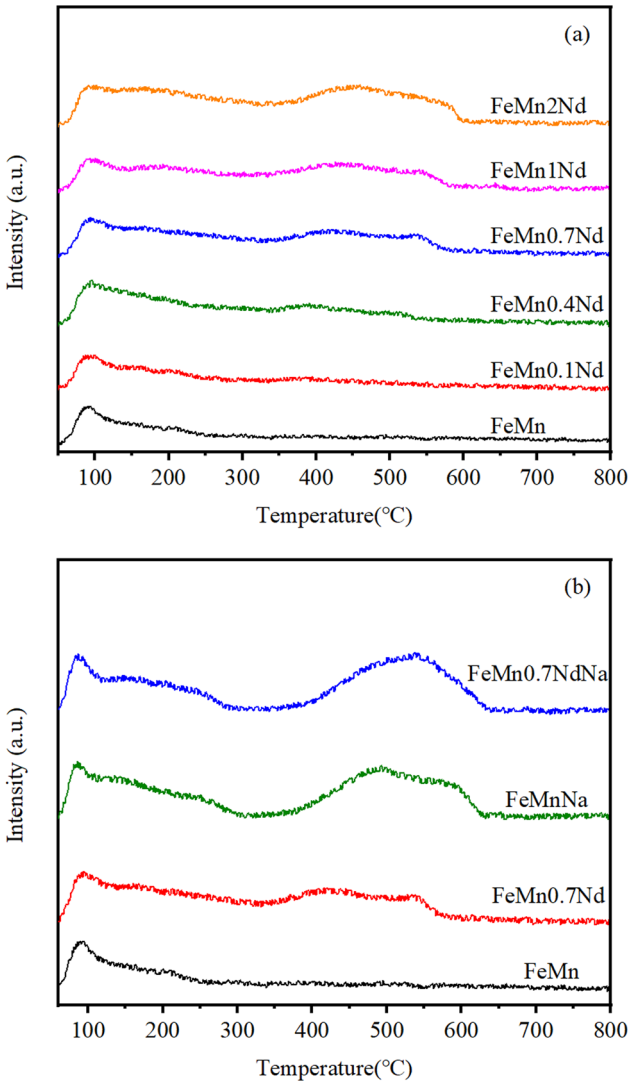

Fig. 7 CO_2-TPD curves of the reduced catalysts.

a plausible explanation for the suppressed hydrogen adsorption lies in the enhanced electron density of iron conferred by Nd modification, thereby limiting the catalyst's ability to adsorb hydrogen species.[27,35] Upon Na incorporation, both FeMnNa and FeMn0.7NdNa show significantly reduced H_α and H_β peak areas relative to FeMn and FeMn0.7Nd. This suggests that Na also exerts a strong inhibitory effect on hydrogen adsorption.

3.4.3. CO_2 chemisorption. CO_2-TPD was employed to evaluate the surface basicity of the reduced catalysts,[9,36] with the corresponding profiles presented in Fig. 7. It is generally accepted that the capacity for CO_2 adsorption correlates positively with the strength and abundance of basic sites on the catalyst surface.[37,38] As shown in Fig. 7, two distinct types of desorption features can be identified for all samples: a low-temperature peak between 100 and 300 °C, attributed to physically adsorbed CO_2, and a high-temperature peak in the range of 400–700 °C, associated with chemically adsorbed CO_2 species.[11,39,40] Examining the effect of Nd promotion (Fig. 7a), a progressive increase in the integrated areas of both the

physical and chemical CO_2 desorption peaks is observed as the Nd content rises from 0 to 2%. Moreover, these desorption features shift toward higher temperatures with increasing Nd loading. These trends indicate that Nd introduction enhances the surface basicity of the catalysts, and that this promoting effect becomes more pronounced at higher Nd contents.

As shown in Fig. 7b, the incorporation of Na into both FeMn and FeMn0.7Nd catalysts leads to a marked increase in the peak areas corresponding to CO_2 physical and chemical desorption, accompanied by a clear shift of these peaks toward higher temperatures. These observations indicate that Na promotion significantly enhances the surface basicity of the catalysts. Remarkably, the co-promoted FeMn0.7NdNa catalyst shows the strongest CO_2 dissociative desorption capability. This observation demonstrates a powerful synergistic effect between Nd and Na, wherein their combined presence further amplifies the surface basicity beyond the levels achieved by either promoter individually.

3.5. Phase composition of the spent catalysts

Mössbauer spectroscopy was employed to identify the iron phases present in the spent catalysts, with the corresponding spectra shown in Fig. S3. The spectra were deconvoluted into one central doublet and multiple sextet components, and the fitted hyperfine parameters are summarized in Table 2. The sextet characterized by a hyperfine field (Hhf) of 476.61 kOe is attributed to the Fe_3O_4 phase. Additional sextets with Hhf values in the ranges of 213.12–217.73 kOe, 182.12–190.20 kOe, and 105.35–110.66 kOe are assigned to χ-Fe_5C_2.[34] Those with Hhf values between 165.73 and 171.61 kOe correspond to ε'-$Fe_{2.2}C$.[41,42] The sextets showing Hhf values of 197.09, 202.81, and 204.40 kOe are identified as θ-Fe_3C.[24] Such species are typically associated with finely dispersed or nanosized particles.[43] In summary, the primary iron phases in the spent catalysts are χ-Fe_5C_2, ε'-$Fe_{2.2}C$, θ-Fe_3C, and Fe_3O_4.

Table 2 indicates that the introduction of Nd promoter significantly alters the phase distribution. Nd promotion substantially enhances the carburization degree of the spent catalysts. Specifically, the content of χ-Fe_5C_2 increases from 41.2% in FeMn to 63.1% in the Nd-modified counterpart, accompanied by a rise in ε'-$Fe_{2.2}C$ from 14.0% to 23.0%. This finding suggests that Nd promotes iron phase carbonization,[44] particularly χ-Fe_5C_2, which is considered the active phase for FTS.[45–47] As the Nd loading increases from 0.1% to 0.7%, the χ-Fe_5C_2 content rises progressively from 63.1% to 79.1%, while the ε'-$Fe_{2.}{}_2C$ content decreases from 23.0% to 4.8%. Although both χ-Fe_5C_2 and ε'-$Fe_{2.2}C$ are considered FTS-active phases, the latter exhibits lower intrinsic activity.[45,48] Combined with XPS and CO-TPD results, the increasing Nd loading from 0 to 0.7% enhances the electron density around surface Fe atoms and strengthens CO dissociative adsorption. This process promotes Fe–C bond formation, thereby favoring the generation of χ-Fe_5C_2. However, a further increase in Nd loading to 2% leads to a decrease in the χ-Fe_5C_2 content from 79.1% to 68.3%. This decline is attributed to excessive Nd deposition, which causes particle growth and aggregation, consequently covering active sites and reducing the content of the active χ-Fe_5C_2 phase.

Table 2 MES data of the catalysts after the reaction

Catalyst	Phase	Hhf (kOe)	IS (mm s^{-1})	QS (mm s^{-1})	Area (%)
FeMn	Fe^{3+}(spm)	—	0.33	1.02	15.0
	Fe_3O_4	476.61	0.37	0.01	29.8
	χ-Fe_5C_2	215.74	0.26	−0.12	25.7
		190.2	0.20	0.18	8.2
		107.32	0.18	0.31	7.3
	ε'-$Fe_{2.2}C$	170.64	0.27	−0.01	14.0
FeMn0.1Nd	Fe^{3+}(spm)	—	0.39	1.07	13.8
	χ-Fe_5C_2	216.66	0.24	−0.12	25.3
		189.81	0.19	−0.01	20.3
		107.8	0.24	0.02	17.5
	ε'-$Fe_{2.2}C$	171.49	0.22	−0.05	23.0
FeMn0.4Nd	Fe^{3+}(spm)	—	0.36	1.02	18.1
	χ-Fe_5C_2	213.12	0.25	−0.09	22.1
		182.12	0.17	−0.04	27.0
		105.35	0.28	−0.01	16.0
	ε'-$Fe_{2.2}C$	165.73	0.23	−0.08	16.7
FeMn0.7Nd	Fe^{3+}(spm)	—	0.27	1.01	16.2
	χ-Fe_5C_2	214.46	0.24	−0.12	28.8
		184.73	0.25	0.12	33.1
		107.67	0.12	0.06	17.2
	ε'-$Fe_{2.2}C$	168.3	0.21	−0.24	4.8
FeMn1Nd	Fe^{3+}(spm)	—	0.36	1.09	16.3
	χ-Fe_5C_2	216.86	0.23	−0.09	28.2
		186.64	0.22	0.03	27.3
		108.81	0.18	0.08	15.9
	θ-Fe_3C	204.4	0.22	−0.07	8.0
	ε'-$Fe_{2.2}C$	169.84	0.20	−0.11	4.3
FeMn2Nd	Fe^{3+}(spm)	—	0.38	1.05	18.7
	χ-Fe_5C_2	216.72	0.23	−0.08	28.0
		186.64	0.16	−0.06	25.3
		110.45	0.23	−0.05	15.0
	θ-Fe_3C	202.81	0.20	−0.03	8.2
	ε'-$Fe_{2.2}C$	171.61	0.22	−0.04	4.9
FeMnNa	χ-Fe_5C_2	217.73	0.25	−0.10	37.0
		182.2	0.18	0	29.6
		108.51	0.20	−0.08	22.1
	θ-Fe_3C	197.09	0.19	0.02	11.2
FeMn0.7NdNa	Fe^{3+}(spm)	—	0.36	1.03	4.3
	χ-Fe_5C_2	216.98	0.25	−0.10	22.9
		185.03	0.21	−0.01	42.7
		110.66	0.23	0.07	16.5
	ε'-$Fe_{2.2}C$	167.57	0.23	−0.09	13.6

Table 2 further reveals the effect of Na promoter. For the FeMnNa catalyst, the addition of Na increases the χ-Fe_5C_2 content dramatically from 41.2% to 88.7%, but also results in the formation of 11.2% θ-Fe_3C. The θ-Fe_3C phase is generally considered inert in iron-based FTS, and its formation is often linked to surface carbon deposition, typically observed in deactivated catalysts.[49–51] In contrast, for the FeMn0.7Nd catalyst, the co-introduction of Na (forming FeMn0.7NdNa) further elevates the χ-Fe_5C_2 content from 79.1% to 82.1%, with no detectable θ-Fe_3C. These findings indicate that while Na promotes the formation of χ-Fe_5C_2, it can also lead to the generation of the inactive θ-Fe_3C phase. Notably, a synergistic interaction between Nd and Na arises from their co-promotion,

which simultaneously suppresses θ-Fe_3C formation and enhances the content of the active χ-Fe_5C_2 phase.

3.6. FTS performance

The results of the FTS evaluation for all catalysts are compiled in Table 3. For the FeMn*x*Nd catalysts, the CO conversion increases from 83.1% to 89.1% as the Nd loading rises from 0 to 0.7%. This enhancement is attributed to the promotional effects of Nd. Synthesizing the results obtained from CO_2-TPD, XPS, CO-TPD, and MES, the introduction of Nd up to 0.7% progressively strengthens the surface basicity, increases the electron density around Fe atoms, and enhances CO dissociative adsorption.

As a consequence of these combined factors, Fe–C bond formation is promoted, the active χ-Fe_5C_2 phase is preferentially generated, and CO conversion is correspondingly increased. Furthermore, BET, XRD, and TEM analyses demonstrate that moderate Nd incorporation progressively increases surface area while decreasing particle size and improving Fe nanoparticle dispersion, all contributing to higher FTS activity. However, a further increase in Nd loading to 2% decreases the CO conversion from 89.1% to 68.5%. Excessive Nd deposition on the catalyst surface induces iron oxide particle agglomeration, resulting in increased particle size, reduced surface area, and coverage of active sites. These morphological changes hinder reactant diffusion, limit reduction and carburization, and ultimately reduce the content of the active χ-Fe_5C_2 phase—accounting for the lower CO conversion.

The CO conversion drops dramatically from 83.1% for FeMn to 24.0% for FeMnNa, highlighting the detrimental effect of Na introduction on catalytic activity. Correlating this with the Mössbauer spectroscopy results, the significant loss in activity can be primarily attributed to the formation of an 11.2% fraction of the inactive θ-Fe_3C phase in FTS. The θ-Fe_3C phase is commonly associated with deactivated iron-based catalysts.[49–51] In contrast, the addition of Na to FeMn0.7Nd (forming FeMn0.7NdNa) further improves the CO conversion from 89.1% to 95.1%. As shown in Fig. S4, significant iron particle agglomeration is observed in the spent FeMnNa catalyst, whereas the spent FeMn0.7NdNa catalyst retains a particulate morphology without obvious aggregation. This indicates that Na alone tends to induce particle agglomeration after reaction, while the co-presence of Nd and Na suppresses the aggregation of Fe species through a synergistic effect, which is also supported by H_2-TPR results. Furthermore, the FeMn0.7NdNa catalyst exhibits the highest CO conversion (95.1%). The synergistic interplay between Nd and Na in FeMn0.7NdNa manifests across multiple characterization domains: enhanced surface basicity (CO_2-TPD), elevated Fe electron density (XPS), and superior CO dissociation (CO-TPD). Crucially, MES reveals that these concerted effects translate into preferential formation of the active χ-Fe_5C_2 phase at the expense of the inactive θ-Fe_3C phase.

As shown in Table 3, the hydrocarbon distribution shifts with increasing Nd loading. As the Nd content rises from 0.1% to 2%, the CH_4 selectivity increases from 36.1% to 41.0%, the C_5^+ selectivity decreases from 17.1% to 8.8%, the C_2^0–C_4^0 selectivity increases from 17.3% to 19.0%, alongside a slight enhancement in light olefins selectivity, which increases from 29.5% to 31.3%. Light olefin yield exhibits a volcanic trend with increasing Nd loading: from 298.4 g h^{-1} kg_{Cat}^{-1} for FeMn, it reaches a peak of 340.4 g h^{-1} kg_{Cat}^{-1} for FeMn0.7Nd, before declining to 273.0 g h^{-1} kg_{Cat}^{-1} for FeMn2Nd. This trend can be explained by two factors: first, H_2-TPD results show that Nd suppresses hydrogen adsorption, thereby favoring olefin formation; second, the FeMn0.7Nd catalyst possesses a high electron density around surface Fe atoms, which enhances CO dissociation and results in a low surface H/C ratio, together with its highest χ-Fe_5C_2 content, collectively promoting light olefin production. These findings align with the report by Zeng *et al.*,[19] who observed that the introduction of Nd shifts the product distribution toward lighter hydrocarbons, increasing selectivity to C_1–C_4 products while suppressing C_5^+ formation.

The introduction of Na to the FeMn catalyst (FeMnNa) enhances C–C coupling capability, as evidenced by increased selectivity to $C_2^=$–$C_4^=$ and C_5^+ hydrocarbons, along with a rise in the O/P ratio from 1.6 to 3.8. However, this comes at the cost of a sharp increase in CH_4 selectivity, which rises from 37.0% to 43.2%—a clear indication of concurrent catalyst deactivation. Characterization by MES and TEM reveals the structural origins of this deactivation: the formation of an inactive θ-Fe_3C phase, accompanied by severe agglomeration of iron particles during

Table 3 Catalytic activity of samples[a]

			Distribution of hydrocarbons (%)						
Catalyst	X_{CO} (%)	S_{CO_2} (%)	CH_4	C_2^0–C_4^0	$C_2^=$–$C_4^=$	C_5^+	O/P	Y ($C_2^=$–$C_4^=$) (g h^{-1} kg_{Cat}^{-1})	C balance (%)
FeMn	83.1	39.6	37.0	18.4	28.9	15.6	1.6	298.4	97.2
FeMn0.1Nd	84.5	39.0	36.1	17.3	29.5	17.1	1.7	312.8	96.6
FeMn0.4Nd	86.3	39.3	38.8	18.6	29.3	13.3	1.6	315.7	97.3
FeMn0.7Nd	89.1	39.3	39.2	18.3	30.6	11.9	1.7	340.4	97.1
FeMn1Nd	72.0	38.4	40.0	18.0	31.8	10.2	1.8	290.1	96.3
FeMn2Nd	68.5	38.1	41.0	19.0	31.3	8.8	1.6	273.0	96.7
FeMnNa	24.0	44.1	43.2	7.6	29.2	19.9	3.8	80.6	96.1
FeMn0.7NdNa	95.1	37.5	21.5	7.1	33.7	37.7	4.7	412.1	97.6

[a] 320 °C, $H_2/CO = 2$, 1.0 MPa, 12 000 mL h^{-1} g_{Cat}^{-1}, 45 h.

FTS. Consequently, a stark contrast is evident in light olefin yield: 298.4 g h^{-1} kg_{Cat}^{-1} for the unpromoted FeMn *versus* a mere 80.6 g h^{-1} kg_{Cat}^{-1} for the Na-modified FeMnNa. In contrast, the introduction of Na to FeMn0.7Nd (forming FeMn0.7NdNa) improves the product distribution markedly: the CH_4 selectivity decreases from 39.2% to 21.5%, the C_2^0–C_4^0 selectivity decreases from 18.3% to 7.1%, while the light olefin selectivity increases to 33.7%, C_5^+ selectivity more than triples to 37.7%, and the O/P ratio reaches 4.7—a nearly threefold increase from 1.7. The synergistic interaction between Nd and Na underpins the superior product selectivity observed for FeMn0.7NdNa. The Nd–Na combination effectively suppresses hydrogen adsorption, limiting secondary hydrogenation of olefins. This synergy simultaneously enhances surface basicity, increases electron density on Fe atoms, promotes CO dissociative adsorption, and enriches the active χ-Fe_5C_2 phase. These properties collectively create an environment with an exceptionally low surface H/C ratio, favoring C–C coupling over hydrogenation and chain termination. Consequently, the catalyst exhibits enhanced selectivity to both light olefins and C_5^+ hydrocarbons, culminating in an impressive light olefin yield of 412.1 g h^{-1} kg_{Cat}^{-1}—far surpassing the yields of singly promoted counterparts (340.4 g h^{-1} kg_{Cat}^{-1} for FeMn0.7Nd and 80.6 g h^{-1} kg_{Cat}^{-1} for FeMnNa).

4. Conclusions

Rare earth metal Nd was introduced into FeMn catalysts *via* a two-step synthesis route involving coprecipitation and impregnation. The role of Nd in modulating the structural, electronic, and catalytic properties of FeMn-based catalysts was systematically evaluated. A range of characterization techniques was employed to probe the effects on textural properties, electronic characteristics, chemisorption behavior, reduction–carburization processes, and FTS performance across the FeMn*x*Nd, FeMnNa, and FeMn0.7NdNa catalyst series.

The introduction of Nd induces favorable structural modifications: Nd reduces catalyst particle size, improves Fe nanoparticle dispersion, and increases BET specific surface area. These textural enhancements collectively promote better dispersion of the active phase, thereby boosting FTS activity. Furthermore, Nd incorporation modulates the electronic and adsorption properties of the catalyst in ways that favor FTS performance. Specifically, it strengthens surface basicity, increases electron density around surface Fe atoms, suppresses hydrogen adsorption, and promotes CO dissociative adsorption. These combined effects facilitate Fe–C bond formation and accelerate the generation of the χ-Fe_5C_2 phase, ultimately leading to enhanced FTS performance. However, excessive Nd loading leads to the deposition of surplus Nd on the catalyst surface, resulting in particle agglomeration, increased particle size, decreased BET surface area, and coverage of active sites. These effects collectively reduce the content of the active χ-Fe_5C_2 phase, ultimately decreasing both CO conversion and light olefin yield. While the sole addition of Na promotes the formation of the χ-Fe_5C_2, it also tends to induce the generation of the inactive θ-Fe_3C phase and causes noticeable particle aggregation after reaction. In contrast, the co-introduction of Nd–Na creates a synergistic effect that not only suppresses the formation of θ-Fe_3C and prevents particle aggregation but also further increases the content of the χ-Fe_5C_2. Benefiting from the Nd–Na synergy, the FeMn0.7NdNa catalyst exhibits enhanced surface basicity, higher electron density around Fe atoms, and stronger CO dissociative adsorption capability, leading to a higher content of the active χ-Fe_5C_2 phase. These attributes contribute to its superior CO conversion and light olefin yield. Notably, the FeMn0.7NdNa catalyst achieves a light olefin yield of 412.1 g h^{-1} kg_{Cat}^{-1}, markedly surpassing that of FeMn0.7Nd and FeMnNa.

Author contributions

Yi Yang: conceptualization, methodology, investigation, writing – original draft, visualization. Fengping Yu: writing – review & editing. Delong Ding: writing – review & editing. Chunliang Ge: writing – review & editing, supervision, funding acquisition. Biao Chen: resources. Xiaojiong Wu: resources. Yaoji Chen: resources. Hanfeng Lu: resources, funding acquisition. Hongfang Ma: resources, funding acquisition. Haitao Zhang: resources, funding acquisition. Weixin Qian: resources, funding acquisition. Weiyong Ying: supervision, funding acquisition.

Conflicts of interest

No conflict of interest exists in the submission of this manuscript.

Data availability

Data is provided within the manuscript or supplementary information (SI). The authors declare that the data supporting the findings of this study are available within the paper and its SI. Supplementary information is available. See DOI: https://doi.org/10.1039/d6ra02950g.

Acknowledgements

This work was supported by the National Key Research and Development Program of China (No. 2022YFC3701502-02), the Key Research and Development Project in Zhejiang Province (No. 2024C03108) and Zhejiang Zheneng Technology & Environment Group Co., Ltd Technology Project (No. ZNKJ-2023-067).

References

1 N. C. Shiba, X. Liu and Y. Yao, *Fuel Process. Technol.*, 2022, **238**, 107489.
2 M. Li, A. Noreen, Y. Fu, C. C. Amoo, Y. Jiang, X. Sun, P. Lu, R. Yang, C. Xing and S. Wang, *Fuel*, 2022, **308**, 121938.
3 Y. Liu, D. Deng and X. Bao, *Chem*, 2020, **6**, 2497–2514.
4 Z. Zhao, Y. Li, H. Zhu, Y. Lyu and Y. Ding, *Chem. Commun.*, 2023, **59**, 3827–3837.

5 R. Dalebout, L. Barberis, N. L. Visser, J. E. S. van der Hoeven, A. M. J. van der Eerden, J. A. Stewart, F. Meirer, K. P. de Jong and P. E. de Jongh, *ChemCatChem*, 2022, **14**, e202200451.
6 L. Sineva, K. Gryaznov, E. Asalieva, S. Urvanov, V. Aksenenkov, N. Batova and V. Z. Mordkovich, *Energy Fuels*, 2026, **40**, 3796–3805.
7 N. C. Shiba, Y. Yao, R. P. Forbes, C. G. Okoye-Chine, X. Liu and D. Hildebrandt, *Fuel Process. Technol.*, 2021, **216**, 106781.
8 F. Yousefian, M. A. Babatabar, M. Eshaghi, S. M. Poor and A. Tavasoli, *Fuel Process. Technol.*, 2023, **247**, 107818.
9 Y. Yang, H. Zhang, H. Ma, W. Qian, Q. Sun and W. Ying, *Fuel*, 2022, **326**, 125090.
10 H. M. T. Galvis, J. H. Bitter, C. B. Khare, M. Ruitenbeek, A. I. Dugulan and K. P. de Jong, *Science*, 2012, **335**, 835–838.
11 Z. Han, W. Qian, H. Zhang, H. Ma, Q. Sun and W. Ying, *Ind. Eng. Chem. Res.*, 2020, **59**, 14598–14605.
12 U. Burgun, H. R. Zonouz, H. Okutan, H. Atakül, S. Senkan, A. Sarioglan and G. Gumuslu Gur, *ACS Omega*, 2023, **8**, 648–662.
13 C. Wang, T. Fan, S. Lv, T. Zhang, J. Zhang and J. Chen, *Fuel*, 2026, **407**, 137581.
14 C. Schmidt, H. Wollmerstädt and S. Kureti, *ChemCatChem*, 2025, **17**, e202400632.
15 W. Zhang, H. Zhang, M. Abbas, J. Zhang, Z. Huang, S. Kawi and J. Chen, *Fuel*, 2024, **363**, 131013.
16 H. Ma, Y. Yang, H. Fu, H. Zhang, W. Qian, Q. Sun and W. Ying, *Fuel*, 2024, **357**, 129605.
17 Y. Yang, W. Qian, H. Zhang, Z. Han, H. Ma, Q. Sun and W. Ying, *Catal. Sci. Technol.*, 2022, **12**, 4624–4636.
18 Y. Yang, H. Zhang, H. Ma, W. Qian, Q. Sun and W. Ying, *Top. Catal.*, 2023, **66**, 508–522.
19 S. Zeng, Y. Du, H. Su and Y. Zhang, *Catal. Commun.*, 2011, **13**, 6–9.
20 C. Nie, H. Zhang, H. Ma, W. Qian, Q. Sun and W. Ying, *Catal. Lett.*, 2019, **149**, 1375–1382.
21 M. Chen, Z. Wang, Q. Lv, C. Li, S. Sun and S. Hu, *J. Hazard. Mater.*, 2018, **341**, 198–206.
22 K. Cheng, M. Virginie, V. V. Ordomsky, C. Cordier, P. A. Chernavskii, M. I. Ivantsov, S. Paul, Y. Wang and A. Y. Khodakov, *J. Catal.*, 2015, **328**, 139–150.
23 X. Guo, L. Guo, Y. Cui, T. Vitidsant, P. Reubroycharoen, G. Liu, J. Wu, Y. Yoneyama, G. Yang and N. Tsubaki, *Catal. Today*, 2021, **375**, 290–297.
24 F. Lu, X. Chen, Z. Lei, L. Wen and Y. Zhang, *Appl. Catal., B*, 2021, **281**, 119521.
25 S. Qin, C. Zhang, J. Xu, Y. Yang, H. Xiang and Y. Li, *Appl. Catal., A*, 2011, **392**, 118–126.
26 M. Gu, S. Dai, R. Qiu, M. E. Ford, C. Cao, I. E. Wachs and M. Zhu, *ACS Catal.*, 2021, **11**, 12609–12619.
27 Z. Han, W. Qian, H. Ma, X. Wu, H. Zhang, Q. Sun and W. Ying, *RSC Adv.*, 2020, **10**, 42903–42911.
28 Z. Liu and P. Hu, *J. Am. Chem. Soc.*, 2001, **123**, 12596–12604.
29 X. Wu, W. Qian, H. Zhang, Z. Han, H. Zhang, H. Ma, D. Liu, Q. Sun and W. Ying, *Catal. Sci. Technol.*, 2021, **11**, 2577–2588.
30 J. Li, X. Cheng, C. Zhang, J. Wang, W. Dong, Y. Yang and Y. Li, *J. Chem. Technol. Biotechnol.*, 2017, **92**, 1472–1480.
31 X. Wu, W. Qian, H. Ma, H. Zhang, D. Liu, Q. Sun and W. Ying, *Fuel*, 2019, **257**, 116101.
32 J. Li, Y. Hou, Z. Song, C. Liu, W. Dong, C. Zhang, Y. Yang and Y. Li, *Mol. Catal.*, 2018, **449**, 1–7.
33 H. Suo, S. Wang, C. Zhang, J. Xu, B. Wu, Y. Yang, H. Xiang and Y. Li, *J. Catal.*, 2012, **286**, 111–123.
34 M. Qing, Y. Yang, B. Wu, J. Xu, C. Zhang, P. Gao and Y. Li, *J. Catal.*, 2011, **279**, 111–122.
35 Z. Ma, H. Ma, H. Zhang, X. Wu, W. Qian, Q. Sun and W. Ying, *ACS Omega*, 2021, **6**, 4968–4976.
36 Y. An, T. Lin, F. Yu, K. Gong, X. Wang, X. Qi, D. Lv, Y. Sun and L. Zhong, *Catal. Sci. Technol.*, 2022, **12**, 2677–2687.
37 X. Su, J. Zhang, S. Fan, Q. Ma and T. Zhao, *RSC Adv.*, 2015, **5**, 80196–80202.
38 H. Wan, B. Wu, Z. Tao, T. Li, X. An, H. Xiang and Y. Li, *J. Mol. Catal. A: Chem.*, 2006, **260**, 255–263.
39 Z. Han, W. Qian, H. Ma, H. Zhang, Q. Sun and W. Ying, *RSC Adv.*, 2019, **9**, 32240–32246.
40 X. Wu, H. Ma, H. Zhang, W. Qian, D. Liu, Q. Sun and W. Ying, *Ind. Eng. Chem. Res.*, 2019, **58**, 21350–21362.
41 X. Liu, Z. Cao, S. Zhao, R. Gao, Y. Meng, J. Zhu, C. Rogers, C. Huo, Y. Yang, Y. Li and X. Wen, *J. Phys. Chem. C*, 2017, **121**, 21390–21396.
42 Z. Tao, Y. Yang, C. Zhang, T. Li, J. Wang, H. Wan, H. Xiang and Y. Li, *Catal. Commun.*, 2006, **7**, 1061–1066.
43 C. Zhang, H. Wan, Y. Yang, H. Xiang and Y. Li, *Catal. Commun.*, 2006, **7**, 733–738.
44 Z. Ma, W. Qian, H. Zhang, H. Ma, Q. Sun and W. Ying, *Fuel*, 2022, **319**, 123613.
45 Q. Chang, C. Zhang, C. Liu, Y. Wei, A. V. Cheruvathur, A. I. Dugulan, J. W. Niemantsverdriet, X. Liu, Y. He, M. Qing, L. Zheng, Y. Yun, Y. Yang and Y. Li, *ACS Catal.*, 2018, **8**, 3304–3316.
46 D. Chun, J. Park, S. Hong, J. Lim, C. Kim, H. Lee, J. Yang, S. Hong and H. Jung, *J. Catal.*, 2014, **317**, 135–143.
47 J. M. Cho, B. G. Kim, G. Y. Han, J. Sun, H. K. Jeong and J. W. Bae, *Fuel*, 2020, **281**, 118779.
48 J. M. Cho, S. R. Lee, J. Sun, N. Tsubaki, E. J. Jang and J. W. Bae, *ACS Catal.*, 2017, **7**, 5955–5964.
49 E. De Smit, F. Cinquini, A. M. Beale, O. V. Safonova, W. van Beek, P. Sautet and B. M. Weckhuysen, *J. Am. Chem. Soc.*, 2010, **132**, 14928–14941.
50 C. Yang, H. Zhao, Y. Hou and D. Ma, *J. Am. Chem. Soc.*, 2012, **134**, 15814–15821.
51 K. Xu, B. Sun, J. Lin, W. Wen, Y. Pei, S. Yan, M. Qiao, X. Zhang and B. Zong, *Nat. Commun.*, 2014, **5**, 5783.